Three-Body Dissociation Dynamics of Excited States of $O_3(D_2O)$

A. K. Luong, T. G. Clements, and R. E. Continetti*

Department of Chemistry and Biochemistry, University of California, San Diego, 9500 Gilman Drive, La Jolla, California 92093-0314

Received: June 15, 1999; In Final Form: August 17, 1999

In these experiments, the dynamics of the three-body dissociative photodetachment of $O_3^-(D_2O)$ at 258 nm are directly probed for the first time. Photodetachment of a negatively charged precursor, with coincident energy analysis of the photoelectron, allows production of energy-selected excited-state $O_3(D_2O)$ complexes. By measurement of the laboratory velocities and recoil angles of the $O + O_2 + D_2O$ products simultaneously, a kinematically complete description of the three-body dissociation dynamics of $O_3(D_2O)$ is obtained. The results show that clustering of D_2O to O_3^- stabilizes the system by 0.75 ± 0.09 eV. Photodetachment to the triplet states of O_3 in the complex results in three-body dissociation, with no clear evidence observed for quenching or intracluster reaction in the complex. The molecular-frame differential cross section (MF-DCS), showing how the three products scatter in the molecular frame, is presented and discussed in light of DFT calculations of possible equilibrium geometries of the parent $O_3^-(D_2O)$ anion.

1. Introduction

The chemistry of tropospheric and stratospheric ozone has stimulated much research interest since the discovery of the impact of ozone in our atmosphere. There remain, however, puzzling issues to be resolved. Two such issues may involve three-body reaction dynamics. Locker et al. and Anderson, et al. suggested that the three-body recombination process $O + O_2 + M \rightarrow O_3 + M$ involving low-lying excited states of ozone may contribute to an understanding of the observed discrepancies between measured and calculated rates of ozone production in the atmosphere.[1,2] In addition, Mauersberger et al. recently proposed an explanation for isotopic fractionation of ozone in the stratosphere based on how the atomic and molecular oxygen collide in the three-body recombination reaction to form ozone, rather than the symmetry of the different isotopomers of ozone itself.[3] The experiments discussed in this paper study the three-body dissociation dynamics of the lowest excited states of O_3 clustered to D_2O. While the present work does not directly probe the three-body recombination process on the ground-state surface, it provides the first insights into the three-body dynamics of the system.

The experimental results for the $O_3(D_2O)$ system will be compared with those for O_3; hence, a brief discussion of relevant O_3 chemistry is in order. Extensive studies have been conducted to understand the electronic spectrum of O_3. At photon energies below 3 eV, the Chappuis and Wulf absorption bands of neutral O_3 have been assigned to several low-lying excited states, three of which are poorly characterized triplet states: $^3A_2$, $^3B_2$, and $^3B_1$. These states have been shown, experimentally and theoretically, to lie slightly above the dissociation asymptote of O_3 to form the ground states of $O + O_2$.[4−8] In a previous experiment in this laboratory, Garner, et al. implemented the photoelectron−photofragment coincidence (PPC) technique to demonstrate that the low-lying excited states of ozone promptly dissociate.[9] In these experiments, the dissociative photodetachment (DPD) of O_3^- that occurs when photodetachment produces an excited state of O_3 was studied by measuring the photoelectron and photofragment kinetic energy and angular distributions in coincidence. The results supported the suggestion that the dissociation proceeds via the antisymmetric stretch, leading to a distortion from C_{2v} to C_s symmetry.[9] A more recent optical spectroscopy experiment conducted by Abel et al. shows lifetimes of 50−100 ps for the lowest triplet excited state of O_3.[10]

In the present experiments, the three-body dissociation of $O_3(D_2O)$ is studied by investigating DPD of the $O_3^-(D_2O)$ complex. Studies of three-body dissociation using the PPC technique are now possible with a new apparatus capable of multiparticle detection, enabling coincidence measurements of a photodetached electron and three or more neutral fragments.[11] This technique has been previously applied to the study of the three-body dissociation dynamics of O_6.[12] When $O_3^-(D_2O)$ is photodetached at 258 nm, an electronically excited ozone−water complex may be formed and undergo the following DPD processes:

$$O_3^-(D_2O) + h\nu \rightarrow O + O_2 + D_2O + e^- \quad (1)$$

$$\rightarrow O_3 + D_2O + e^- \quad (2)$$

$$\rightarrow 2OD + O_2 + e^- \quad (3)$$

In reaction 1, photodetachment of the anion precursor yields an excited $O_3(D_2O)$ complex that undergoes dissociation to $O + O_2 + D_2O$. This is the analogue of the process studied by Garner et al. in free O_3.[9] The dissociation of excited O_3 is quenched in reaction 2, producing stable O_3 and D_2O. Reaction 3 involves an intracluster reaction between the dissociating ozone and water moieties to form two hydroxyl radicals, which has been suggested to play a role in the formation of OH in the troposphere.[13,14]

The PPC technique used in these experiments records the kinetic energy, mass, and angular distributions of an electron and three photofragments in coincidence. The complete kine-

* To whom correspondence should be addressed. E-mail: rcontinetti@ucsd.edu.

10.1021/jp991975c CCC: $18.00
Published on Web 09/29/1999

matic characterization of a DPD event provided by this method allows one to differentiate among the possible reaction channels. Previous optical studies of the neutral ozone−water complex used ultraviolet excitation of the higher-lying singlet excited states to promote the intracluster reaction following optical excitation and compared the results to the gas-phase $O + H_2O$ reaction.[15−17] In the present investigation, photodetachment of the $O_3^-(D_2O)$ anion is used to prepare and study the dissociation dynamics of the low-lying excited states of the neutral cluster, providing the first direct insights into the three-body dissociation dynamics of $O_3(D_2O)$. In the following sections, the experimental approach and results are presented. Density functional theory calculations of the structure of $O_3^-(D_2O)$ complex are also reported to complement the experimental observations.

2. Experimental Section

The apparatus has been previously described in detail and will only be briefly described here.[11,12] The spectrometer consists of four differentially pumped regions: the source, acceleration, time-of-flight, and interaction−detection regions. The apparatus allows production of fast, mass-selected negative-ion beams and photodetachment with electron energy analysis. An efficient multiparticle detector is used to record kinetic energy and angular distributions in three-body dissociation processes.

Ozone is generated using a commercial electric-discharge ozonator and is stored on silica gel at −78 °C until use. During the experiment, the temperature of the ozone trap is raised and maintained at approximately −45 °C by use of an FTS Systems chiller. Neat oxygen is flowed through the trap, and the source and carrier gas mixture is passed over chilled D_2O (5 °C) and into a piezoelectric pulsed valve. $O_3^-(D_2O)$ and other anions are generated by intersecting a 1 kHz pulsed supersonic expansion of the source gas with a 1 keV electron beam. The ions are accelerated to 4 keV, mass-selected, guided into the interaction region, and intersected by a focused, linearly polarized laser beam. The 1 kHz laser pulse is taken from the third harmonic (258 nm, 4.80 eV) of the Ti:sapphire fundamental at 775 nm (1.2 ps fwhm) generated by a CPA2000 regenerative amplifier (Clark-MXR, Inc.) and focused to a 0.5 mm diameter spot at the interaction region to give a fluence of approximately 5−10 mJ/cm^2 per pulse.

Photodetached electrons are detected by one of two time- and position-sensitive wedge-and-strip-anode electron detectors, which are placed opposite each other and perpendicular to the ion beam path. The use of a fast ion beam and the large distribution of flight paths in the large-solid-angle photoelectron detector leads to a significant broadening in the laboratory electron kinetic energy spectrum. To deal with this broadening, the photoelectron detector measures the laboratory kinetic energy by recording the recoil angle (by position of arrival at the detector) and time of arrival of the electron. The component of the electron kinetic energy due to the ion beam velocity is subtracted from the measured laboratory kinetic energy, and a correction for the actual flight path is then made during analysis of the data. The center-of-mass (CM) electron kinetic energy (eKE) determined in this way gives a resolution of $\Delta E/E \approx$ 5% at 1.3 eV and peak position to about ±0.01 eV.

Residual ions remaining in the beam after the interaction region are electrostatically deflected from the beam path to an ion detector, providing a means of monitoring the ion beam intensity. Neutral photofragments leaving the interaction volume continue to fly over a 1.04 m flight distance until they impinge on a time- and position-sensitive multiparticle detector, allowing determination of the recoil velocities of three or more (up to eight) particles in coincidence. This heavy particle detector is made up of four quadrants, each of which is a separate crossed-delay-line detector. This detector has been demonstrated to yield a photofragment translational energy resolution of ∼15% $\Delta E/E$ at 0.7 eV in studies of the three-body dissociation of O_6^- and effectively has no dead regions within the active diameter of the detector.[11]

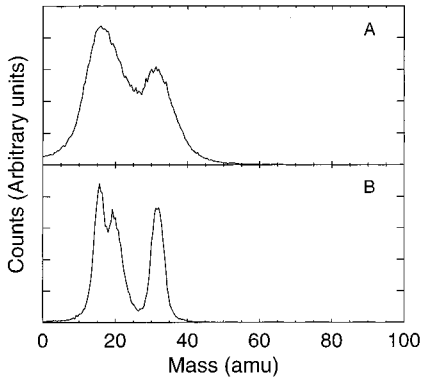

Figure 1. The calculated raw mass spectrum for $O_3(D_2O)$ is shown in frame A. In frame B, the mass resolution is improved by narrowing the centroid distributions of the events accepted in the data analysis as discussed in the text.

2.1. Data Analysis. Since the electron and all photofragments are measured in coincidence, the correlated kinetic energy and angular distributions of all the products are recorded in one experiment. During data analysis, events are sorted by the number of particles detected. All recorded events that yield one electron and at least one heavy particle are analyzed to obtain the photoelectron spectrum, N(eKE), at a given wavelength. Events that produce one electron and two neutral photofragments, and one electron and three neutral photofragments are analyzed as correlated information for two- and three-body dissociation events, respectively. Statistics based on spectrometer efficiency and count rate of the experiment ensure that the photoelectron and photofragments from each event are correlated. Under the conditions of this experiment, a typical rate for correlated three-body dissociations of 0.13 events per laser shot results in false coincidences of ∼2%. Similarly, a typical rate of 0.29 two-body dissociation events per laser shot yields an estimated ∼6.6% false coincidence rate.[18]

For analysis of three-body dissociation, the laboratory frame velocities are determined from the known CM velocity of the incident ion beam and the time- and position-of-arrival of the detected particles. The calculated laboratory frame velocities are then transformed into a CM frame with one of the particles along the positive x-axis. By use of the known parent mass and conservation of linear momentum, the masses of the three photofragments can be calculated.[11] The mass spectrum for three-body dissociation events found for the $O_3(D_2O)$ system is shown in Figure 1A, which does not provide enough resolution to differentiate between reaction channels 1 and 3. Energetic considerations, discussed below, rule out any significant contributions from reaction channel 3. The mass resolution can be improved by narrowing the distribution of event centroids accepted in the data analysis by a factor of 3 (from ±3 mm to ±1 mm in x, y, and z about the nominal beam center), allowing the O_2 fragment to be cleanly resolved from the overlapping O and D_2O peaks as demonstrated in Figure 1B. Note that the variation in the peak heights is due to a mass-dependent variation in the peak widths. To remove any remaining ambiguity in the data analysis, the lightest fragment is assigned to the O atom

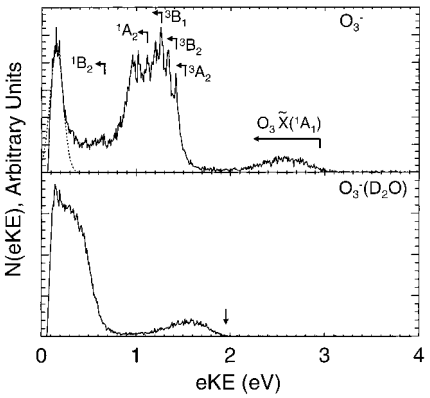

Figure 2. Photoelectron spectra, N(eKE), for O_3^- and $O_3^-(D_2O)$ are shown in upper and lower frames, respectively. These spectra were collected at 258 nm and represent all events producing one photoelectron and at least one neutral particle. A fit to the laser-related background signal at low eKE was obtained and is shown as a dashed line in the spectra. The arrow in the lower frame shows the maximum eKE used to calculate the electron affinity of $O_3(D_2O)$.

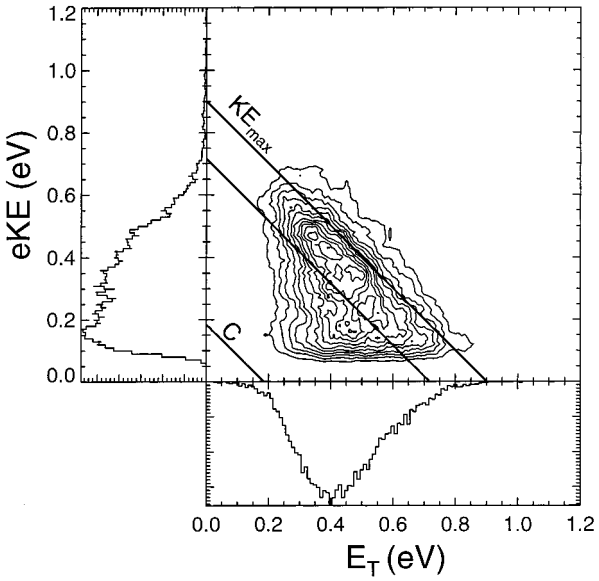

Figure 3. $N(E_T,\text{eKE})$ correlation spectrum for $O_3^-(D_2O)$ at 258 nm. The evenly spaced contours represent the number of events with the specified values of E_T and eKE. The three diagonal lines from top to bottom are the maximum translational energy available to the products $O(^3P) + O_2(^3\Sigma_g^-,v=0,1) + D_2O + e^-$ and $2OH + O_2(^3\Sigma_g^-,v=0) + e^-$ (labeled C).

and the next lightest to D_2O. The photofragment masses and CM velocities are then used to determine the kinetic energy of each fragment, which can then be simply summed to give the CM translational energy (E_T) released in the three-body dissociation process.

To visualize the dynamics of the three-body decay process, an image of the molecular-frame differential cross section (MF-DCS) can be constructed. Hsieh et al. and Lavollée et al. have implemented similar visualization schemes to study the dynamics of three-body dissociation of doubly charged cations.[19,20] The MF-DCS is obtained by transforming the data for each event from the laboratory frame to a CM molecular breakup frame such that the particle with the smallest mass recoils along the positive x-axis. Because of the limited mass resolution shown in Figure 1, this results in some mixing of the assignment of the O and D_2O fragments. Because of the similar masses of these particles and the relatively low translational energy resolution of the multiparticle detector, this has a negligible effect on the measured product E_T distributions. It does have an effect on the MF-DCS, however, and in the MF-DCS presented here, the further assumption has been made that the O atom is the fastest particle. This will be discussed further in section 3.4 below.

3. Results and Discussion

3.1. Photoelectron Spectra. Figure 2 shows the N(eKE) spectra of O_3^- and $O_3^-(D_2O)$. These spectra were recorded at 258 nm, with the laser polarization parallel to the ion beam path. The spectra are composed of events yielding one photoelectron and at least one neutral particle. There are two broad features in the photoelectron spectrum of O_3^-, both of which have been previously assigned.[5] The higher kinetic energy feature is due to photodetachment of O_3^- $\tilde{X}(^2B_1)$ to the O_3 $\tilde{X}(^1A_1)$ ground state, and the lower kinetic energy feature is from photodetachment to the low-lying excited states of ozone as noted in the figure. A sharp feature near 0 eV is due to an electron background created from the scattering of the 258 nm laser beam off detector surfaces, and a Gaussian fit of this feature is shown in the figure as a dashed curve. In the lower frame, the photoelectron spectrum of $O_3^-(D_2O)$ exhibits two similar features shifted to lower eKE. The second feature at lower eKE is superimposed on the electron background noise near 0 eV. The similarity of the features in the O_3^- and $O_3^-(D_2O)$ photoelectron spectra suggests that the electron is localized on O_3 in the complex and that there are negligible charge-transfer-to-solvent effects.

A Gaussian fit of the higher eKE feature in the $O_3^-(D_2O)$ spectrum, originating from photodetachment to the electronic ground state of $O_3(D_2O)$, shows a shift to lower eKE of 0.85 ± 0.04 eV. This is chiefly a measure of the significant stabilization of O_3^- through interaction with D_2O and suggests that the electron affinity (EA) of $O_3(D_2O)$ is 2.95 ± 0.04 eV. Two-body dissociation, with a small kinetic energy release of $\sim$0.1 eV, was observed to occur predominantly in coincidence with photodetachment to the ground electronic state of the $O_3(D_2O)$ complex. Approximately 3% of the two-body events are observed to be correlated with photodetachment to the low-lying excited states of $O_3(D_2O)$. However, in light of the estimated $\sim$6.6% false coincidence rate for two-body dissociation, this is insignificant, leading to the conclusion that quenching of the low-lying excited states of O_3 by clustering with D_2O followed by two-body dissociation or formation of a stable complex is a minor channel at best.

These observations show that vertical photodetachment of the anion does not occur to a bound region of the potential energy surface. This means that the location of the features in the photoelectron spectra are shifted to lower eKE and that the number quoted here thus represents an upper bound of the adiabatic EA of $O_3(D_2O)$. A second effect to be considered in the evaluation of the adiabatic EA is the stabilization of $O_3(D_2O)$ relative to $O_3 + D_2O$. This has previously been estimated to be in the range 0.03−0.10 eV.[21,22] Taking into account an average value for the stability of the neutral cluster relative to ozone, the adiabatic EA found above can be adjusted downward to give an upper bound of 2.88 ± 0.04 eV for $O_3(D_2O)$. This is consistent with a binding energy of $O_3^-(D_2O)$ relative to $O_3^- + D_2O$ of $\sim 0.78 \pm 0.04$ eV.

3.2. Photoelectron−Photofragment Correlation Spectra. Figure 3 illustrates the CM photoelectron−photofragment kinetic energy correlation spectrum of $O_3^-(D_2O)$. Integration over either E_T or eKE yields the N(eKE) and $N(E_T)$ spectra along the y-

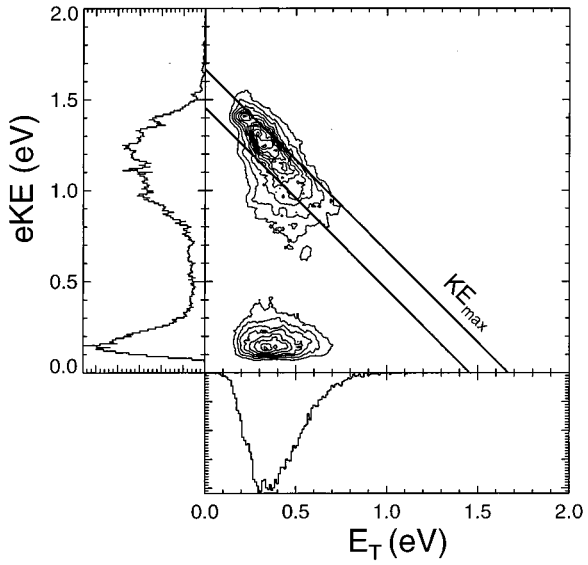

Figure 4. $N(E_T,\text{eKE})$ spectrum for O_3^- at 258 nm. From top to bottom, the two diagonal lines represent the maximum translational energy available to the products $O(^3P) + O_2(^3\Sigma_g^-,v=0,1) + D_2O + e^-$.

and *x*-axes, respectively. The contours in the spectrum represent the number of events, $N(E_T,\text{eKE})$, exhibiting that particular distribution of energy among the photoproducts. As discussed above, no three-body dissociation events correlated with the ground state of the $O_3(D_2O)$ complex were observed. Thus, the $N(E_T,\text{eKE})$ spectrum for $O_3^-(D_2O)$ is only shown up to 1.2 eV along the eKE and E_T axes.

The shape of the $N(E_T,\text{eKE})$ spectrum of $O_3^-(D_2O)$ is similar to that previously observed for O_3^-,[9] with the exception of the large shift in eKE discussed above. For comparison, the $N(E_T,\text{eKE})$ spectrum of O_3^- at 258 nm is shown in Figure 4. The two diagonal lines drawn at higher energies in Figure 4 indicate the maximum amount of translational energy available (KE_{max}) for formation of an electron and ground-state $O + O_2$ ($v = 0$ or 1), given the photon energy, the known bond dissociation energy,[23] and the EA of O_3.[24] As noted by Garner et al.,[9] the features in the contour map near the KE_{max} line in Figure 4 indicate that photodetachment of O_3^- to the $^3A_2$ and $^3B_2$ excited states of O_3 produces fragments with most of the available energy deposited into translational rather than internal degrees of freedom. However, photodetachment of O_3^- to the next higher excited states of O_3, $^3B_1$, and $^1A_2$ leads to photofragments with more rotational and/or vibrational energy in the O_2. Assuming that vibrational excitation in the parent $O_3^-(D_2O)$ is negligible and that the partitioning of energy in the dissociation is similar to O_3^-, a value of $KE_{max} = 0.90 \pm 0.09$ eV can be found from the diagonal line in Figure 3. The uncertainty is estimated from the measured energy resolution of the photofragment and photoelectron detectors. Owing to the absence of resolved features in the photoelectron spectrum of $O_3^-(D_2O)$, the structure observed in the O_3^- $N(E_T,\text{eKE})$ spectrum is not observed in Figure 3.

Examination of the $N(E_T)$ spectra for O_3^- and $O_3^-(D_2O)$ in Figure 5 shows that the partitioning of energy into product translation is remarkably similar, providing further justification for the location of the KE_{max} line in the $O_3^-(D_2O)$ $N(E_T,\text{eKE})$ spectrum. In fact, the $N(E_T)$ spectrum for $O_3^-(D_2O)$ peaks at ~0.40 eV, 0.05 eV higher than the spectrum for O_3^-. Examination of the photoelectron and correlation spectra show that this shift is due to a diminished contribution from photodetachment to the lowest-lying excited states, $^3A_2$ and $^3B_2$, of O_3 in the cluster. Energy conservation and the observed partitioning of

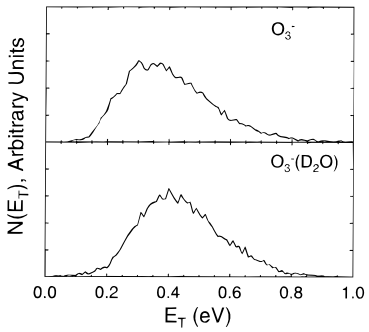

Figure 5. $N(E_T)$ spectra for O_3^- and $O_3^-(D_2O)$.

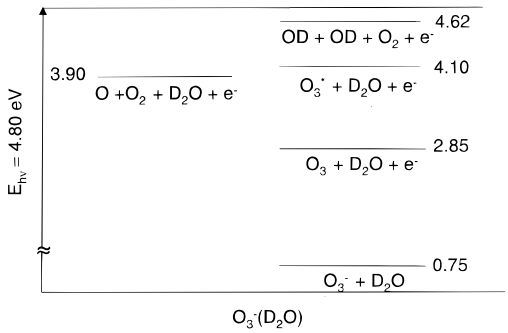

Figure 6. Energetics of the DPD of $O_3^-(D_2O)$ at 258 nm. The energetics of the OD + OD + O_2 + e^- channel is determined using $\Delta_f H°(0K)$ for OD, O_2, and D_2O.

energy in O_3^- dictates that photodetachment to these states yields higher eKE photoelectrons and lower E_T photofragments. The photoelectron spectrum of $O_3^-(D_2O)$ in Figure 2 shows that no resolved features attributable to these states are present in the photoelectron spectrum and that the photoelectron spectrum rises relatively slowly in the region where these states should contribute. This may be due to a shift in the Franck−Condon overlap between the anion cluster and the lowest triplet excited states of $O_3(D_2O)$ compared to O_3.

3.3. Energetics of $O_3^-(D_2O)$ and $O_3(D_2O)$. The results presented here allow construction of an energetics diagram for the $O_3^-(D_2O)$ system as shown in Figure 6. When the value of KE_{max} is subtracted from the photon energy at 258 nm (4.80 eV), a value of 3.90 ± 0.09 eV is obtained for the minimum energy for DPD of $O_3^-(D_2O)$. Combining this number with the known dissociation energy[23] and EA for O_3 [24] yields a value of 0.75 ± 0.09 eV for the bond dissociation energy of $O_3^-(D_2O) \rightarrow O_3^- + D_2O$. This value is in good agreement with the upper bound determined from the comparison between the $N(\text{eKE})$ spectra of O_3^- and $O_3^-(D_2O)$ (0.78 ± 0.04 eV). The energetics dictate that if an intracluster reaction were to occur after photodetachment at 258 nm, the maximum translational energy available to the OD + OD + O_2 products would be 0.18 eV.[25] In Figure 3, this line is labeled C, below which no features are observed. Thus, photodetachment of $O_3^-(D_2O)$ to the low-lying excited states of O_3 in the neutral cluster at 258 nm yields only ground-state atomic and molecular oxygen and water as a three-body dissociation:

$$O_3^-(D_2O) + h\nu \rightarrow O(^3P) + O_2(^3\Sigma_g^-) + D_2O + e^- \quad (4)$$

3.4. Molecular-Frame Differential Cross Section. As discussed in section 2.1, to show the relative scattering of the three photofragments in the molecular frame, the MF-DCS for three-body dissociation is generated by transforming the momentum vectors of all three particles from the laboratory to a

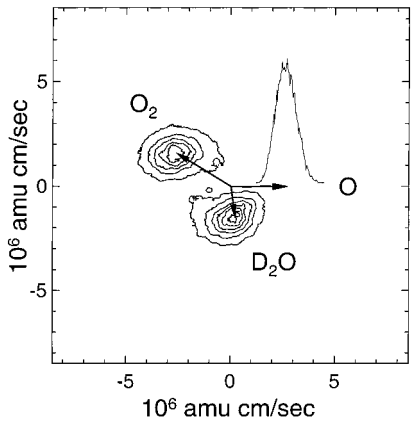

Figure 7. MF-DCS for $O_3(D_2O)$ at 258 nm, represented in a two-dimensional histogram of the number of particles scattered with a specific CM recoil momentum. The contours are evenly spaced. The O atom is chosen to lie along the *x*-axis, the O_2 photofragments are plotted above the *x*-axis, and the coincident D_2O photofragments are plotted below the *x*-axis. The curve above the vector drawn for the O atom shows the distribution of the O atom recoil momenta along the *x*-axis.

TABLE 1: Parameters for the Calculated Minimum Energy Structures for H_2O, O_3, and O_3^- Using B3PW91/6-311++G(d,p)[a]

	energy (hartree)	bond length (Å)	bond angle (deg)
H_2O	−76.428	0.960 (*0.957*)	104.82 (*104.51*)
O_3	−225.39	1.247 (*1.272*)	118.53 (*116.7*)
O_3^-	−225.485	1.340 (*1.342*)	115.68 (*112.6*)

[a] The numbers in parentheses are experimental values.[24,28]

CM molecular frame. Because of the limited mass resolution, O and D_2O cannot be fully resolved in this experiment, so the further assumption is made in generation of the MF-DCS that the O atom is the fastest particle. Because all three momentum vectors lie in one plane, a two-dimensional histogram of all the events can be generated such that the perpendicular component of the momentum of each particle is along the *y*-axis and the parallel component along the *x*-axis. Figure 7 shows the histogram of the MF-DCS in momentum space for $O_3(D_2O)$, where the arrows represent the momentum vectors from the CM of the molecular breakup frame to the centroids of each feature. These vectors show that the centroid of the O_2 distribution recoils backward relative to the O atom, while the centroid of the D_2O feature is actually observed to be slightly forward-scattered relative to the recoiling O atom. The striking result from the MF-DCS is that the product momenta are partitioned such that the heaviest fragment, O_2, carries away most of the momentum, with the lighter O and D_2O fragments recoiling in the other direction in the CM. This observation is unaffected by the assumption that the O atom is the fastest particle. If this assumption is not used, the only significant change observed is that the O and D_2O distributions become bimodal. It should be noted that the MF-DCS plot in Figure 7 is not selected for total energy available to the neutral particles by gating on the eKE. In cases when the N(eKE) or $N(E_T)$ spectra are more resolved to show distinctive features for the different electronic states accessed by photodetachment, selective eKE or E_T gating in the MF-DCS may provide additional insights into the dissociation dynamics.

3.5. Structure of $O_3^-(D_2O)$ and Three-Body Dissociation Dynamics of $O_3(D_2O)$. Given the weak interaction between D_2O and neutral O_3, once the $O-O_2$ bond begins to break after excitation to the excited states of O_3, the subsequent dissociation

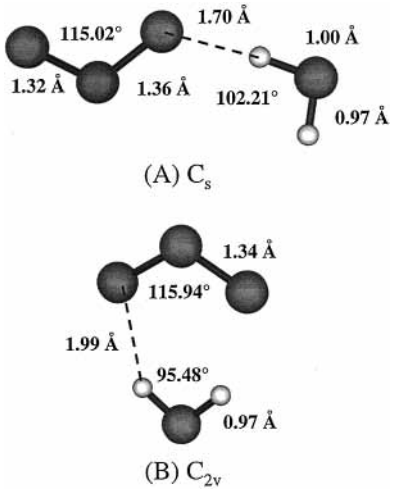

Figure 8. Calculated minimum energy geometries using DFT for $O_3^-(H_2O)$ were found to have (A) C_s and (B) C_{2v} symmetries. This figure was prepared using MacMolPlt: Bode, B. M.; Gordon, M. S. *J. Mol. Graphics Model.*, in press.

is expected to occur rapidly relative to the time scale of molecular rotation. Thus, the observed anisotropy in the MF-DCS may be correlated with the geometry of the nascent neutral cluster produced by photodetachment. To gain further insights into the meaning of the observed partitioning of momentum among O_2, O, and D_2O in the MF-DCS, it is valuable to consider possible structures for $O_3^-(D_2O)$ that would dictate the Franck−Condon region accessed in the neutral complex by photodetachment. By use of density functional theory (DFT) as implemented in Gaussian 94,[26] a geometry search for the possible structures of the $O_3^-(H_2O)$ complex was conducted. Since the theoretical calculations are based on the Born−Oppenheimer approximation, there are only negligible differences in using hydrogen or deuterium to determine the geometry of the complex. The method and basis set used, B3PW91/6-311++G(d,p), was chosen on the basis of successful calculations of small oxygen cluster anions by Chertihin and Andrews.[27] Table 1 is a tabulation of the energies and optimized geometries for O_3, O_3^-, and H_2O at this level of theory. The calculations do not perform well for determining the EA of O_3, finding EA = 2.597 eV, which is significantly larger than the experimental value of 2.103 eV.[24] The bond lengths and bond angles, however, are reasonable.[28] Since the primary goal is to determine the possible structures of the anionic cluster, this DFT method provides a reasonable approach. Figure 8 illustrates two calculated minima on the $O_3^-(H_2O)$ potential energy surface. The C_s complex is lower in energy by 0.1 eV and is found to be stabilized relative to $O_3^- + D_2O$ by 0.8 eV, in surprising agreement with the experimental value. However, given the poor performance of the calculations to determine the EA of O_3^-, the small difference in energies between the C_s and C_{2v} complexes is insignificant and cannot be used to determine which structure is more likely to occur.

By use of the MF-DCS in conjunction with the DFT calculations, the most likely geometry of the complex at the time of the molecular breakup may be deduced. In the structure with C_s symmetry, the cluster only forms one hydrogen−oxygen interaction between the two monomers. The calculated C_s geometry indicates that the O−H bond in the water moiety and the $O-O_2$ bond nearest the intracluster interaction are both longer than their respective ground-state bond lengths, consistent with an ion−dipole interaction between the two moieties. The observed breaking of the C_{2v} symmetry of O_3 in the cluster may

be expected to promote the antisymmetric stretch dissociation of the lengthened $O-O_2$ bond. Furthermore, Garner, et al. previously observed that in the DPD of O_3^-, nearly all the available energy appears in translation of the photofragments, particularly for the lowest excited states of O_3.[9] On the basis of this result, which is also observed for $O_3(D_2O)$ in the present study, it was suggested that the transition state for ozone dissociation has a nearly linear configuration. A hypothetical transition-state geometry consistent with the observed dynamics would have a more linear dissociating O_3 moiety pointed toward the O atom in D_2O. In this scenario, D_2O lies in the path of the O atom recoil when the $O-O_2$ bond that was lengthened in the cluster breaks. A significant fraction of the momentum imparted to the O atom is then transferred to D_2O because of the similar masses of these two products, with the heavier O_2 carrying away most of the momentum as it recoils in the other direction. The fact that the partitioning of energy into translation for the three-body dissociation is very similar to free O_3 indicates that the interaction between O and D_2O must be predominantly elastic.

A similar qualitative analysis of the C_{2v} symmetry complex shown in Figure 8 with respect to the observed MF-DCS suggests that this is an unlikely structure for the complex at the time of three-body decay. Assuming once again that the O_3 molecule evolves to a more linear configuration prior to dissociation, recoiling O and O_2 would be expected to have very little interaction with the "spectator" D_2O. It is difficult to imagine how dissociation of the ozone moiety in this structure could result in significant momentum transfer to D_2O or lead to the observed partitioning of momentum with O_2 carrying away the largest fraction. Further assessment of the three-body dynamics, using either classical trajectories or quantum mechanical wave packet calculations, is desirable. A study of this type was recently published by Woywod et al. in an examination of the role of the singlet excited states of O_3 in the Chappuis absorption band.[29] Carrying out such dynamics calculations on the triplet states of O_3 and $O_3(D_2O)$ complexes will require a significant effort to characterize the triplet state potential energy surfaces.

In light of the observed dynamics, the proposed mechanism for dissociation of the complex involving antisymmetric stretch dissociation of a more linear O_3 transition state appears reasonable. Zittel et al.[30] and Takahashi et al.[31] demonstrated that the photodissociation cross section for production of $O(^1D)$ from higher-lying singlet states in the Huggins and Hartley bands is highly correlated with the ν_3 antisymmetric stretch mode. Additionally, Garner, et al. suggested that the bond angle of the low-lying $^3A_2$ and $^3B_2$ excited states increases to form a nearly linear geometry before dissociation.[9] The DFT calculations presented here show that the C_{2v} symmetry of O_3 is broken in the most stable anion cluster, leading to a lengthening of one of the O−O bonds. Thus, in photodetachment of the anion complex, the interaction with D_2O shifts the resulting neutral cluster to a geometry closer to the transition state for dissociation of O_3 via the antisymmetric stretch. This may promote a more rapid dissociation of O_3 in the neutral complex relative to free O_3. It will be of interest to obtain higher-resolution photoelectron spectra of the complex to assess if the lack of vibrational resolution in photodetachment to excited states of the complex is in fact governed by the reduction in excited-state lifetime from this perturbation of O_3.

4. Conclusion

These experiments on the DPD of $O_3^-(D_2O)$ provide insights into the energetics of the anion and the three-body dissociation dynamics of excited electronic states of the neutral complex. The results indicate that the clustering of a water molecule to O_3^- stabilizes the system by approximately 0.75 ± 0.09 eV, with an upper bound to the electron affinity of $O_3(D_2O)$ of 2.88 ± 0.04 eV. Photodetachment to the triplet states of O_3 in the complex leads to three-body dissociation, with no clear evidence observed for intracluster reaction or quenching of the excited states in the complex at the level of excitation used in this experiment. In addition, the MF-DCS shows that the partitioning of momentum among the products leads to most of the momentum carried away by O_2, with O and D_2O recoiling in the opposite direction in the CM. When the observations made from the MF-DCS and theoretical calculations are combined, it is possible to make structural inferences on the dissociating neutral complex and the precursor anion. The results are most consistent with an $O_3^-(D_2O)$ complex of C_s symmetry found by DFT calculations. Examination of isotope effects in the three-body dissociation dynamics of ozone−water clusters will be pursued in future experiments in this laboratory.

Acknowledgment. This work was supported by the Air Force Office of Scientific Research under Grant F49620-96-1-0220 and DURIP Grant F49620-97-1-0255. A.K.L. is supported by an AFOSR AASERT Grant F49620-97-1-0387. R.E.C. is a Camille Dreyfus Teacher-Scholar, an Alfred P. Sloan Research Fellow, and a Packard Fellow in Science and Engineering.

References and Notes

(1) Locker, J. R.; Joens, J. A.; Blair, E. J. *J. Photochem.* **1987**, *36*, 235.
(2) S. M. Anderson, S. M.; Mauersberger, K. *J. Geophys. Res.* **1995**, *100*, 3033.
(3) Mauersberger, K.; Erbacher, B.; Krankowsky, D.; Günther, J.; Nickel, R. *Science* **1999**, *283*, 370.
(4) Anderson, S. M.; Mauersberger, K. *J. Geophys. Res.* **1995**, *100*, 3033.
(5) Arnold, D. W.; Xu, C.; Kim, E. H.; Neumark, D. M. *J. Chem. Phys.* **1994**, *101*, 912.
(6) Bouvier, A. J.; Bacis, R.; Bussery, B.; Churassy, S.; Inard, D.; Nota, M.; Brion, J.; Malicet, J.; Anderson, S. M. *Chem. Phys. Lett.* **1996**, *255*, 263.
(7) Tsuneda, T.; Nakano, H.; Hirao, K. *J. Chem. Phys.* **1995**, *103*, 6520.
(8) Borowski, P.; Fulscher, M.; Malmqvist, P.; Roos, B. O. *Chem. Phys. Lett.* **1995**, *237*, 195.
(9) Garner, M. C.; Hanold, K. A.; Resat, M. S.; Continetti, R. E. *J. Phys. Chem. A* **1997**, *101*, 6577.
(10) Abel, B.; Charvát, A.; Deppe, S. F. *Chem. Phys. Lett.* **1997**, *277*, 347.
(11) Hanold, K. A.; Luong, A. K.; Clements, T. G.; Continetti, R. E. *Rev. Sci. Instrum.* **1999**, *70*, 2268.
(12) Hanold, K. A.; Luong, A. K.; Continetti, R. E. *J. Chem. Phys* **1998**, *21*, 9215.
(13) Buckley, P. T.; Birks, J. W. *Atmos. Environ.* **1995**, *25*, 2049.
(14) Frost, G. J.; Vaida, V. *J. Geophys. Res., D: Atmos.* **1995**, *100*, 18803.
(15) Sauder, D. G.; Stephenson, J. C.; King, D. S.; Casassa, M. P. *J. Chem. Phys.* **1992**, *97*, 952.
(16) King, D. S.; Sauder, D. G.; Casassa, M. P. *J. Chem. Phys.* **1994**, *100*, 4200.
(17) Hurwitz, Y.; Naaman, R. *J. Chem. Phys.* **1995**, *102*, 1941.
(18) Continetti, R. E. *Photoionization and Photodetachment*; Ng, C. Y., Ed.; Advanced Series in Physical Chemistry; World Scientific: Singapore, in press.
(19) Hsieh, S.; Eland, J. H. D. *J. Phys. B* **1997**, *30*, 4515.
(20) Lavollée, M.; Bergeron, H. *J. Phys. B: At. Mol. Opt. Phys.* **1992**, *25*, 3101.
(21) Schriver, L.; Barreau, C.; Schriver, A. *Chem. Phys.* **1990**, *140*, 429.
(22) Gillies, J. Z.; Gillies, C. W.; Juenram, R. D.; Lovas, J. F.; Schmidt, T.; Cremer, D. *J. Mol. Spectrosc.* **1991**, *146*, 493.
(23) Gole, J. L.; Zare, R. N. *J. Chem. Phys.* **1972**, *57*, 5331.
(24) Wang, L. J.; Woo, S. B.; Helmy, E. M. *Phys. Rev. A* **1987**, *35*, 759.

(25) Chase, M. W., Jr.; Davies, C. A.; Downey, J. R., Jr.; Frurip, D. J.; McDonald, R. A.; Syverud, A. N. *J. Phys. Chem. Ref. Data* **1985**, *14* (Suppl. 1).

(26) Frisch, M. J.; Trucks, G. W.; Schlegel, H. B.; Gill, P. M. W.; Johnson, B. G.; Robb, M. A.; Cheeseman, J. R.; Keith, T.; Petersson, G. A.; Montgomery, J. A.; Raghavachari, K.; Al-Laham, M. A.; Zakrzewski, V. G.; Ortiz, J. V.; Foresman, J. B.; Cioslowski, J.; Stefanov, B. B.; Nanayakkara, A.; Challacombe, M.; Peng, C. Y.; Ayala, P. Y.; Chen, W.; Wong, M. W.; Andres, J. L.; Replogle, E. S.; Gomperts, R.; Martin, R. L.; Fox, D. J.; Binkley, J. S.; Defrees, D. J.; Baker, J.; Stewart, J. P.; Head-Gordon, M.; Gonzalez, C.; Pople, J. A. *Gaussian 94*, revision E.2; Gaussian, Inc.: Pittsburgh, PA, 1995.

(27) Chertihin, G. V.; Andrews, L. *J. Chem. Phys.* **1998**, *108*, 6404.

(28) Lide, D. R., Ed. *CRC Handbook of Chemistry and Physics*, 76th ed.; CRC Press: Boca Raton, FL, 1995.

(29) Woywod, C.; Stengle, M.; Domcke, W.; Flöthmann, H.; Schinke, R. *J. Chem. Phys.* **1997**, *107*, 7282.

(30) Takahashi, K.; Kishigami, M.; Taniguchi, N.; Matsumi, Y.; Kawasaki, M. *J. Chem. Phys.* **1997**, *106*, 6390.

(31) Zittel, P. F.; Little, D. D. *J. Chem. Phys.* **1980**, *72*, 5900.